そのうちAlexanderら[9]が提唱したparallel loop modelが最も有名なものである。これは大脳皮質とくに前頭葉皮質の異なる部位からの線維連絡が線条体・視床を（多シナプス性に）経由して再び大脳皮質の同じ部位に投射するとする考え方で、当時はあたかもループ間の情報交換がなく独立して並列処理されているようなものと捉えられ大きな議論が起こった。近年は、上述したようにサル脳での大脳皮質から視床への逆行性線維や、視床から線条体への逆行性線維の発見など[8]により、お互いのループは、従来考えられてきたような閉鎖的(closed loop)ではなく開放的(open loop)であるという考えに変わってきている。Alexanderがparallel loop modelを提唱した当時、心理学や人工知能の分野でも並列分散処理モデル(parallel distributed processing model[10])が注目されはじめたが、このモデルも並列処理間は独立でなく「ゆるやかに制約し合いながら」同時処理するという考えが基本にある#。

小生は線条体と大脳皮質との間の線維連絡性に注目している。サルの大脳皮質前頭葉のBrodmann 9野は、複数の研究者（Brodmann, Vogt, Walkerら）により再現性高く同定されている皮質領域であるが、この部位からprobabilistic tractographyを行うことで尾状核、被殻、視床内側部、中脳腹側、脳梁など複数の場所で、同一個体におけるマンガン(Mn)を用いた神経線維追跡法と非常によく一致した結果が得られた（図5A)。マンガンは神経細胞に取り込まれて軸索流により遠位に運ばれるanterograde tracerなので[11]、diffusion-based probabilistic tractographyが皮質・深部灰白質間の神経線維連絡を十分な感度と特異性をもって追跡可能であることを示している。

またヒトでもBrodmann 9野の線条体連絡部位が相同的に位置するか調べるため複数のヒト剖検脳から作成されたヒト脳標準空間内Brodmann 9野(population-based BA9)[12]からの線維連絡を評価した結果も、サルと同様にヒトも尾状核・被殻の背吻側部に最も強い線維連絡が終始することが分かった（図5B)。実際に前頭葉を中心とした皮質をサル・ヒト間で相同的に5領域に分けてこれら区画と線条体内の各画素間の線維連絡性を計算すると、ヒト・サルともに皮質線維が線条体内でtopographicalに分布し両種間で類似していた（図6)。

4. 今後の展開と臨床応用

Diffusion-based tractographyによるヒト脳内の線維連絡性の評価は未だ撮像や解析技術の面から進歩が望まれる。高解像度の角度のMPGによる画像収集、画素内の交差性線維の推定モデルの導入などにより、今後より高感度の方法ができてくると思われる。しかし単一画素内の拡散性が如何に正確に捉えられたとしても現在の拡散強調MRIの解像度は通常ミリメートルの単位でしか収集できず、単一神経線維の径(マイクロメートル単位)に及ばない。そのため画素内で線維が交差しているのか、折れ曲がった線維が接しているだけなのかの

この辺りは心理学者守一雄氏による解説本[14]が分かりやすく面白い。

区別は不可能である。そのため交差線維の推定感度が上がるにつれ「線維連続性」に関する情報を別の手法で補うことも必要と思われる。また前述のように「線維の方向性（神経細胞→軸索末端又は軸索末端→神経細胞）」の評価はできない。

近年 MRI 装置の高磁場(3 テスラ)化やマルチコイル化が進み高 SN 比、短時間で歪みの少ない画像収集が DTI 領域でも期待されている。一方 MPG は強力であるほど拡散運動に感度が高いため、より高い b 値（MPG の強さの指標）での撮像が望ましいがその場合磁場変動の安全性の問題が関わってくる。特に q-ball 法は角度 200 方向以上でより高い b 値を含めた収集が望まれるため安全面からヒトに応用しにくい。Tractography の解析モデルと並行した撮像技術開発も望まれる。

DTI をどのように神経内科領域で応用できるか未だ全貌は見えないが、①多くの神経変性疾患が特定の深部灰白質核の変性を伴うこと、②大脳皮質・深部灰白質間の線維連絡性の定量的評価が可能になってきたこと、から少なくとも神経変性疾患の病態研究に応用できると考えられる。しかし上述のようにこの方法は常に精度・再現性ともに十分な検討が必要である。動物脳で神経線維追跡トレーサーを用いることで「線維連続性」や「線維の方向性」を確認することもその一つの方法であろう。

謝辞
本稿の一部は厚生労働省科学研究費・こころの健康科学(kokoro-H17-025)の支援を受けた。また DTI シーケンス開発に尽力いただいた佐藤博司（国循研・先進診断機器開発室）、浦山慎一（京大・高次脳機能研究センター）、MRI 撮像・解析に協力いただいた花川隆、福山秀直（京大・高次脳機能研究センター）、山本明秀、渡部浩司、寺本昇、飯田秀博（国循研・放医）各氏に深謝する。DTI 解析にはオックスフォード大学脳機能 MRI センターの開発したソフトウェア(FSL, http://www.fmrib.ox.ac.uk/fsl/)の diffusion toolbox (FDT)を使用した（FSL はフリーのソフトウェアで研究用に使用できる）。

参考文献

1. Beaulieu C. The basis of anisotropic water diffusion in the nervous system - a technical review. NMR Biomed 2002;15(7-8):435-55.

2. Basser PJ, Mattiello J, LeBihan D. MR diffusion tensor spectroscopy and imaging. Biophys J 1994;66(1):259-67.

3. Mori S, Crain BJ, Chacko VP, et al. Three-dimensional tracking of axonal projections in the brain by magnetic resonance imaging. Ann Neurol 1999;45(2):265-9.

4. Behrens TE, Woolrich MW, Jenkinson M, et al. Characterization and propagation of uncertainty in diffusion-weighted MR imaging. Magn Reson Med 2003;50(5):1077-88.

5. Klingler J. Erleichterung der makroskopischen Praparation des Gehirns durch den Gefrierprozess. Schweiz Arch Neurol 1935;36:247-256.

6. Morel A, Magnin M, Jeanmonod D. Multiarchitectonic and stereotactic atlas of the human thalamus. J Comp Neurol 1997;387(4):588-630.

7. Behrens TE, Johansen-Berg H, Woolrich MW, et al. Non-invasive mapping of connections between human thalamus and cortex using diffusion imaging. Nat Neurosci 2003;6(7):750-7.

8. Haber S, McFarland NR. The place of the thalamus in frontal cortical-basal ganglia circuits. Neuroscientist 2001;7(4):315-24.

9. Alexander GE, DeLong MR, Strick PL. Parallel organization of functionally segregated circuits linking basal ganglia and cortex. Annu Rev Neurosci 1986;9:357-81.

10. Rumelhart DE, McClelland JL, The-PDP-Research-Group. Parallel Distributed Processing: MIT press; 1986.

11. Sloot WN, Gramsbergen JB. Axonal transport of manganese and its relevance to selective neurotoxicity in the rat basal ganglia. Brain Res 1994;657(1-2):124-32.

12. Rajkowska G, Goldman-Rakic PS. Cytoarchitectonic definition of prefrontal areas in the normal human cortex: II. Variability in locations of areas 9 and 46 and relationship to the Talairach Coordinate System. Cereb Cortex 1995;5(4):323-37.

13. Yasargil MG, Ture U, Yasargil DCH. Surgical anatomy of supratentorial midline lesion. Neurosurgical Focus 2005;18(6b):E1.

14. Johansen-Berg H, Behrens TE, Sillery E, et al. Functional-Anatomical Validation and Individual Variation of Diffusion Tractography-based Segmentation of the Human Thalamus. Cereb Cortex 2004.

15. Kemp JM, Powell TP. The cortico-striate projection in the monkey. Brain 1970;93(3):525-46.

図説明文

図 1 ダツ（魚の一種）の嗅神経、三叉神経、視神経における拡散異方性

嗅神経(A)、三叉神経(B)、視神経(C)における神経線維方向（●）および垂直方向（○）に拡散強調傾斜磁場をかけたときの NMR 信号（横軸は傾斜磁場強度の指標 b 値、縦軸は信号強度を示す）。また各神経の電顕像をそれぞれ D, E, F に示す。 嗅神経は無髄、三叉神経、視神経は有髄神経で、それぞれの神経線維径も違うが垂直方向の NMR 信号強度は 3 神経で同じように低下する。G: 実際にこのデータから q-space 法によって水分子移動確率分布を計算した結果。３本の神経線維ともに平行方向（右）に比べ垂直方向（左）で明らかに拡散移動が制限されているが 3 神経間にはほとんど差がない（実線：嗅神経、破線：三叉神経、点線：視神経）。（文献[1]より改変）

図 2 ヒトにおける巨視的神経線維連絡性。

A-B) Klingler 法による剖検脳の神経線維連絡。右大脳半球内側面(A)から、脳幹部、帯状回皮質、脳梁の内側部が剥離され放線冠（rcc）が露出したところ（B)。黒線の範囲の拡大図を右下に示す（文献[13]より改変)。

C) DTI による画素毎の diffusion tensor の主軸方向。尾状核頭部を通る T1 強調矢状断面上に DTI 画像解析により得られた tensor の主軸方向を赤線で投射したもの。黒線の範囲の拡大図を右下に示す。隣あう画素の主軸方向があたかも神経線維束に沿うように繋がって見えることがわかる。MPG 方向８１方向、空間解像度 2mm で収集し一画素 1.2mm の立方体で再構成した画像データから tensor を計算した。

図 3　Diffusion-based probabilistic tractography で観察した視床亜核からの神経線維連絡

A) 外側膝状体からの線維連絡をたどったもの。一次視覚野に投射する視放線が見える。B) 同じく外側膝状体から側頭葉内側部を迂回して視覚野に投射する視覚路（Mayer's loop）や上丘腕(Brachium)も観察される。C）視床背内側核からの神経線維連絡。背外側の前頭前野(1)および側頭葉内側部(2)に投射する神経線維を追うことができる。D)視床背外側核からの神経線維連絡。一次運動野および小脳皮質への連絡が観察される。（文献[7]より改変）

図 4　Diffusion-based probabilistic tractography による線維連絡性に基づいた視床内の分離。

A) 視床内の各画素を皮質区分（との線維連絡性に基づいて区分したもの。剖検脳による結果（i, ii）と相同的な分離構造が観察される。B)個人毎の視床内分離。C)複数の個人の脳から得られれた標準空間内における tractography に基づいた視床区分。S1/S2: 一次・二次感覚野、M1：一次運動野、PMC：前運動野、PFC：前頭前野、temp：側頭葉、PPC：後部頭頂葉、OCC：後頭葉（文献[14]より改変）

図 5　Brodmann 9 野（BA9）からの線維連絡性。

A）サル脳における線維連絡。Diffusion-based probabilistic tractography (DBPT)によって左BA9からの線維連絡が脳梁、尾状核、被殻、視床内側部、中脳黒質へ伸びていた。これら結果はマンガン(Mn)による神経線維追跡法の結果と良く一致していた。
B）ヒト・サルにおけるBA9の線維連絡性の線条体内分布。最大線維連絡性および線条体の輪郭を矢状面に投射して表示した結果。両種とも尾状核頭部、被殻頭側に投射している。右にBA9の領域を示す。

図6　ヒト・サルでの線条体内の皮質線維連絡分布
サル（右）・ヒト（左）において前頭葉を中心とした皮質を５区分に分け、それら皮質と線条体内の各画素間の線維連絡性を算出し、最大線維連絡性を色分けして表示した結果。両種とも、被殻では皮質からの線維が最も近い被殻内部にtopographicalに分布していた（closest rule [15]）。VMC: 帯状回・眼窩前頭皮質、AFC: 前頭極、MFC: 前頭前野、PMC：前運動野、SM1、傍中心構皮質（一次運動感覚野）。

図 1.

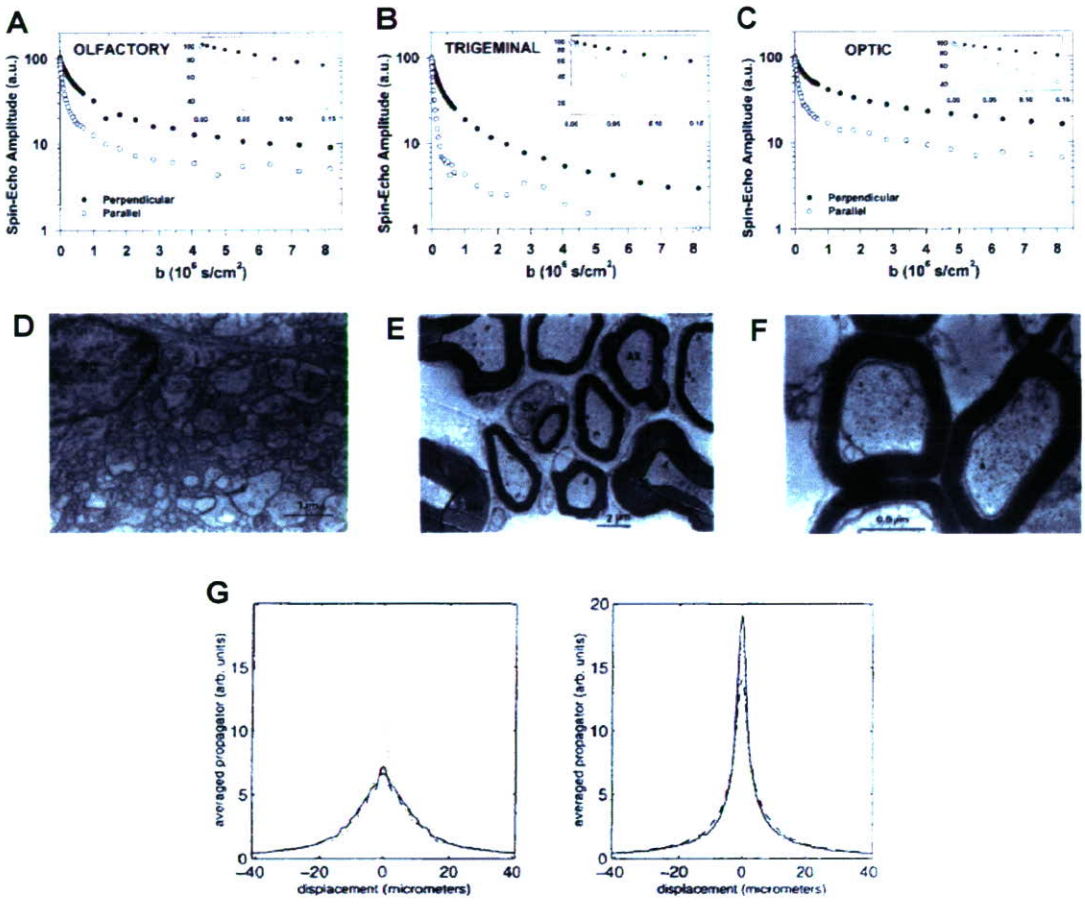
A
OLFACTORY
B
TRIGEMINAL
C
OPTIC
Spin-Echo Amplitude (a.u.)
b (10^6 s/cm^2)
Perpendicular
Parallel
D
E
F
G
averaged propagator (arb. units)
displacement (micrometers)

図 2.

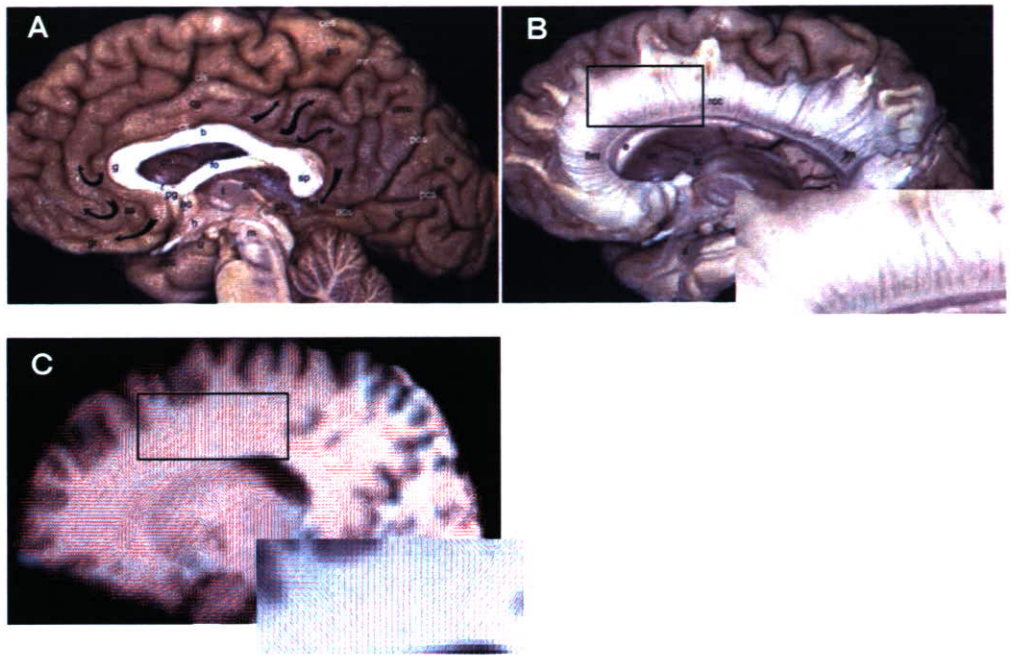

図 3.

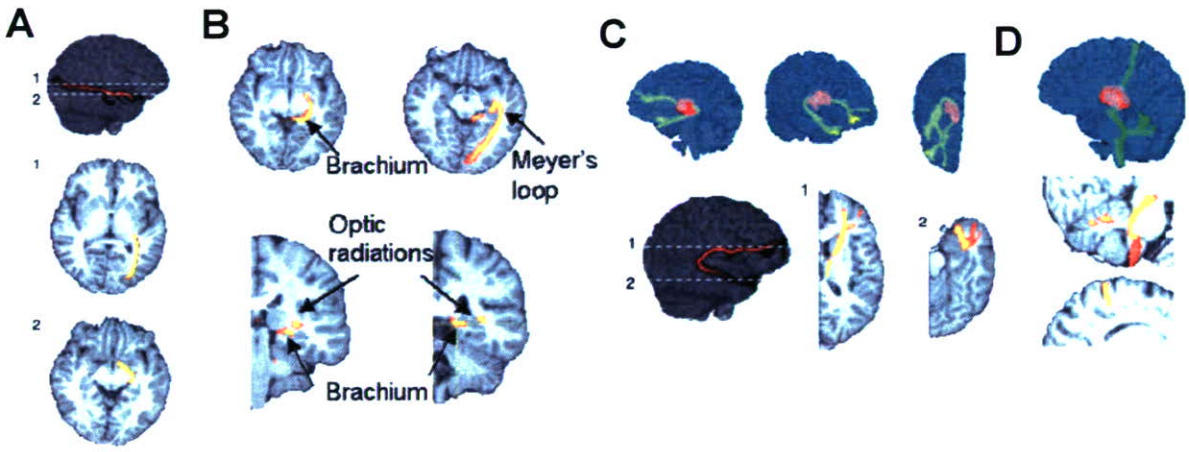
A
B
C
D
1
2
1
2
Brachium
Meyer's
loop
Optic
radiations
Brachium
1
2
1
2

図 4.

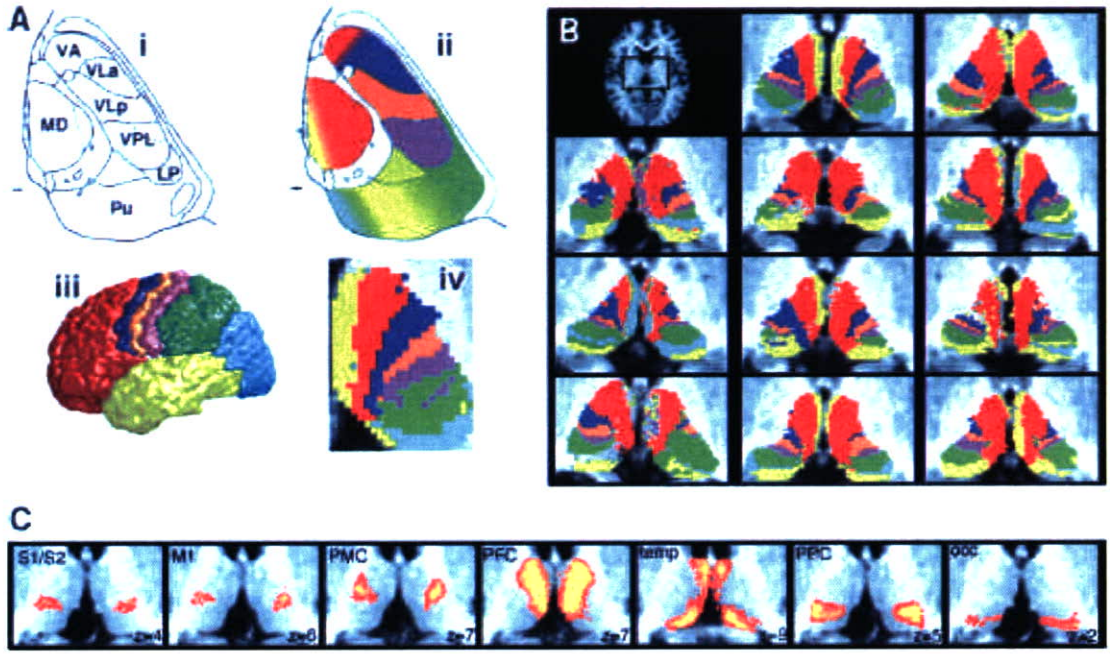
A
i
VA
VLa
VLp
MD
VPL
LP
Pu
ii
iii
iv
B
C
S1/S2
M1
PMC
PFC
temp
PPC
occ

図 5.

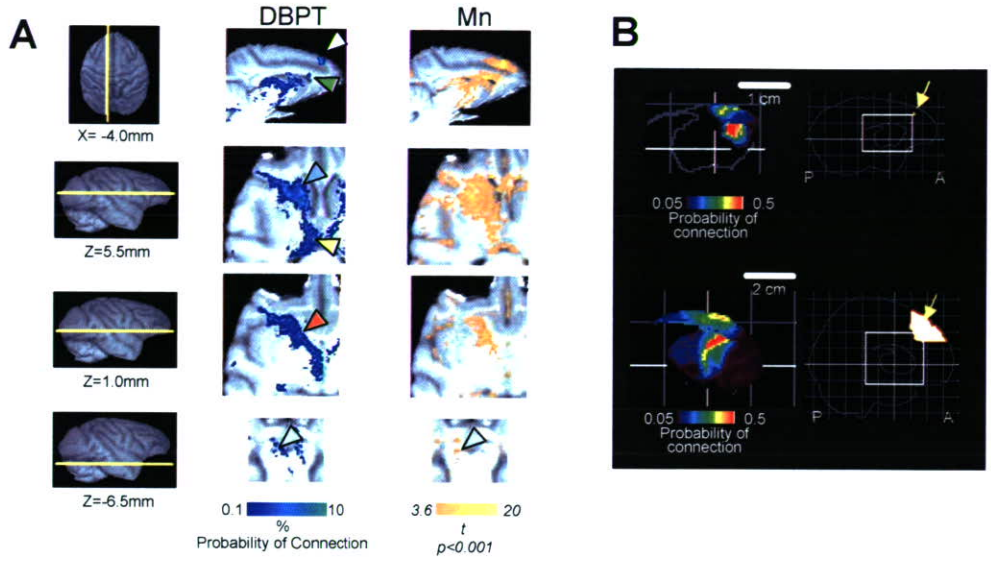
A
DBPT
Mn
X= -4.0mm
Z=5.5mm
Z=1.0mm
Z=-6.5mm
0.1
10
%
Probability of Connection
3.6
20
t
p<0.001
B
1 cm
0.05
0.5
Probability of connection
P
A
2 cm
0.05
0.5
Probability of connection
P
A

図 6.

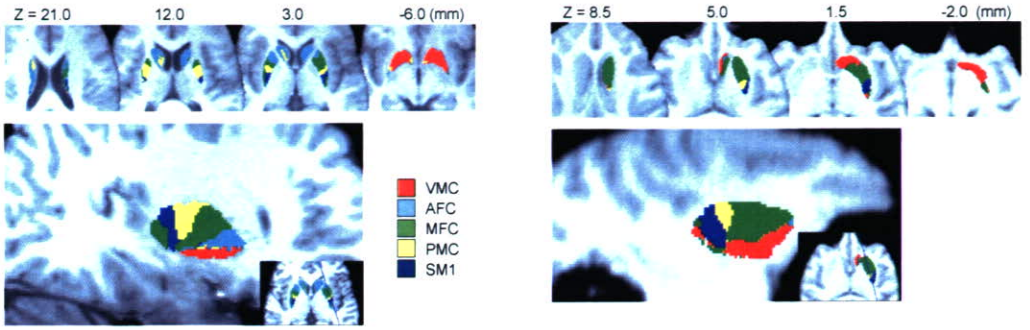

ORIGINAL ARTICLE

Annals of Nuclear Medicine Vol. 20, No. 9, 605–613, 2006

Predicting human performance by channelized Hotelling observer in discriminating between Alzheimer's dementia and controls using statistically processed brain perfusion SPECT

Miho SHIDAHARA,* Kentaro INOUE,* Masahiro MARUYAMA,** Hiroshi WATABE,*** Yasuyuki TAKI,* Ryoi GOTO,* Ken OKADA,* Shigeo KINOMURA,* Shinichiro OSAWA,* Yoshimi ONISHI,**** Hiroshi ITO,* Hiroyuki ARAI***** and Hiroshi FUKUDA*

*Department of Radiology and Nuclear Medicine, Institute of Development, Aging and Cancer, Tohoku University
**Department of Geriatric and Respiratory Medicine, Tohoku University School of Medicine
***Department of Investigative Radiology, National Cardio-vascular Center Research Institute
****Section for Medical Image Information Systems, Research Center for Frontier Medical Engineering, Chiba University
*****Department of Geriatric and Complementary Medicine, Center for Asian Traditional Medicine Research, Tohoku University School of Medicine

Objective: We compared the diagnostic accuracy achieved by a human observer (nuclear medicine physician) and a channelized Hotelling (CH) observer on the basis of receiver-operating characteristics (ROC) curve for the differential diagnosis of Alzheimer's disease (AD) from SPECT images. ***Methods:*** The I-123-IMP brain perfusion SPECT images of 42 subjects (21 AD patients and 21 healthy controls) were used for an interpretation study and those of 10 healthy subjects were for a normal database. SPECT images were processed into four types: original SPECT images, three-dimensional stereotactic surface projection (3DSSP) images derived from them, Z-scores of SPECT images, and Z-scores of 3DSSP images. Five nuclear medicine physicians evaluated the test dataset sequentially as to whether the presented images were those of AD patients, which were rated using five categories of certainty: definitely, possibly, equivocally, possibly not, and definitely not. The test statistics (λ) of the dataset generated by the CH observer were rated for ROC analysis. The areas under the ROC curves (Az) for the four image types interpreted by the human and CH observers were estimated and compared. ***Results:*** Among the four image types, the best performance based on Az obtained by both the CH and human observers was observed for the Z-score of 3DSSP images, and the lowest was for the original SPECT images. ***Conclusions:*** The performance of the CH observer was similar to that of the human observers, and both were dependent on the image type. This indicates that the CH observer may predict human performance in discriminating Alzheimer's dementia and can be useful for comparing and optimizing image processing methods of brain perfusion SPECT without human observers.

Key words: channelized Hotelling observer, Alzheimer's disease, single-photon emission tomography, ROC analysis, three-dimensional stereotactic surface projection

INTRODUCTION

RECENTLY, new medications such as cholinesterase inhibitors have been reported to effectively delay Alzheimer's disease (AD) progression.[1] This finding has increased the importance of an early diagnosis of AD. Thus, over the past several years, much effort has been made to detect AD and to improve the detection of AD on interpretation of brain perfusion SPECT.[2–12] For instance,

Received May 22, 2006, revision accepted August 29, 2006.
For reprint contact: Miho Shidahara, Ph.D., Department of Radiology and Nuclear Medicine, Institute of Development, Aging and Cancer, Tohoku University, Seiryou-machi 4–1, Aoba-ku, Sendai, Miyagi 980–8575, JAPAN.
E-mail: sidahara@idac.tohoku.ac.jp

the statistical manipulation of SPECT images after reconstruction and anatomical standardization makes it easier for a radiologist to detect subtle changes.[6,7,9] The Z-score of three-dimensional stereotactic surface projection (3DSSP) images also adds information regarding cortical perfusion even in very early stages of AD.[10–12]

The receiver-operating characteristics (ROC) analysis by human observers is often used to assess the benefits of newly developed diagnostic techniques.[8–11] Conventionally, interpretation by human observers has been the standard for assessing the detection performance of any algorithm. However, human-observer studies are difficult and time-consuming. Therefore, an alternative method using a mathematical "model," such as a channelized Hotelling (CH) observer, has been developed to assess the effect of image processing (e.g., filter cutoff frequency and scatter compensation strategies).[13–18] A CH observer is characterized as having a psychophysiologic basis in the frequency-selective channels of the human visual system and is expected to predict human performance in image interpretation.[14]

A good agreement between the CH observer (or a similar numerical model) and a human observer for myocardial and hepatic SPECT imaging was reported previously.[18–21] Sankaran et al. reported that the reference index for the performance of defect detection, that is, the area under the ROC curve (Az), is slightly higher for the CH observer than for the human observer, but was marginally within 1 S.D. of human Az for all combinations of attenuation, detector response, and scatter corrections for myocardial SPECT images.[18] Gifford et al. reported that the CH observer in tumor detection by ^{67}Ga SPECT gives a good quantitative agreement with human data sets obtained from two image reconstruction strategies, Filtered-Back Projection (FBP) and Order Subset Expectation Maximization (OS-EM).[21] These studies were aimed at evaluating the diagnostic accuracy of a CH observer compared with a human observer for different image reconstruction and processing protocols. The results suggest that a CH observer may be used as an approximation of a human observer for various detection tasks. The CH observer, however, has not been validated for the assessment of statistically processed brain perfusion images.

The goal of this study was to compare human and CH observers through ROC curves to detect the perfusion pattern characteristic of AD on SPECT images. In this study, we investigated the effects of three frequency cutoff channel models of CH observers.

MATERIAL AND METHODS

Subjects

Brain perfusion SPECT images of 52 subjects were analyzed (AD patients, n = 21; healthy volunteers as controls, n = 31). In the patient group, there were 6 males and 15 females, with a mean age of 69.3 ± 6.3 years (range, 51–75). They were clinically diagnosed by geriatric physicians as having probable AD on the basis of NINCDS-ADRDA criteria.[22] Their averaged Mini Mental State Examination (MMSE) score was 21.6 ± 2.1 (range, 17–26).[23] The controls comprised 15 males and 16 females, with a mean age of 64.9 ± 6.27 years (range 54–74). They were participants in a research program on brain aging in city dwellers conducted by the Institute of Development,

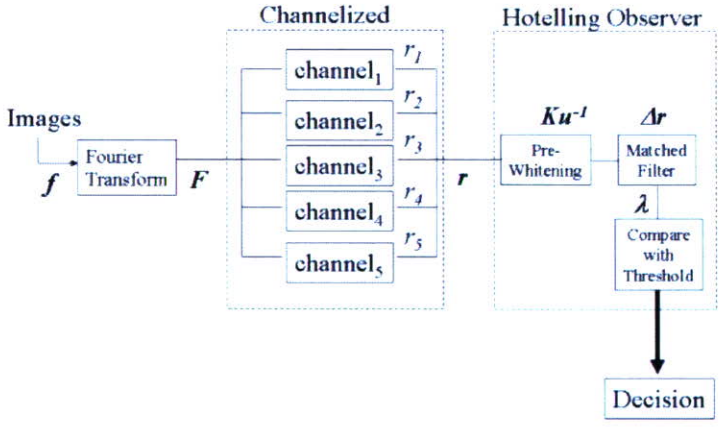

Fig. 1 Schematic diagram of a CH observer. Image **f** was first converted by Fourier transformation. In frequency domain, filtering was applied for Fourier transformed image **F** using radially symmetric channels $\mathbf{u}_c$ and then the channel matrix **r** was obtained (named as Channelized process). The channel matrix **r** was processed by pre-whitening ($\mathbf{K_t}^{-1}$) and matched filter ($\Delta\mathbf{r}$) and then finally, test statistic λ was obtained. The test statistic λ was diagnosed using threshold λ_{thresh}, whether the input image **f** falls in one group or the other (named as Hotelling observer process). Character of Hotelling observer is the use of averaged matrix from the two-covariance matrices derived from channel matrices for one group or the other for $\mathbf{K_t}$ matrix.

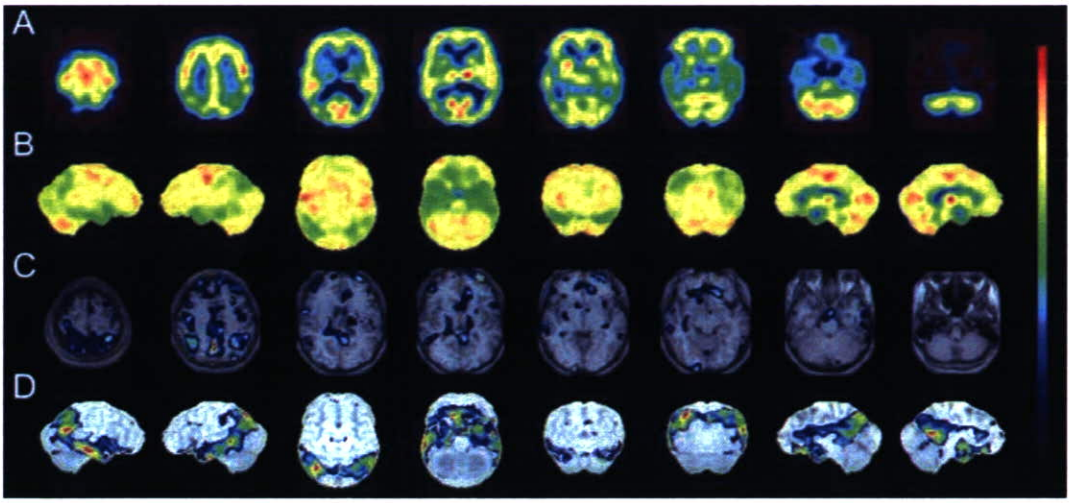

Fig. 2 Representative SPECT images (A), 3DSSP images (B), Z-scores of SPECT images (C) and Z-scores of 3DSSP images (D) used for image interpretation experiment. Images in (B) and (D) are, from left to right, right lateral, left lateral, superior, inferior, anterior, posterior, right mid-sagittal, and left mid-sagittal views. Images in (C) and (D) were superimposed on template MR images.

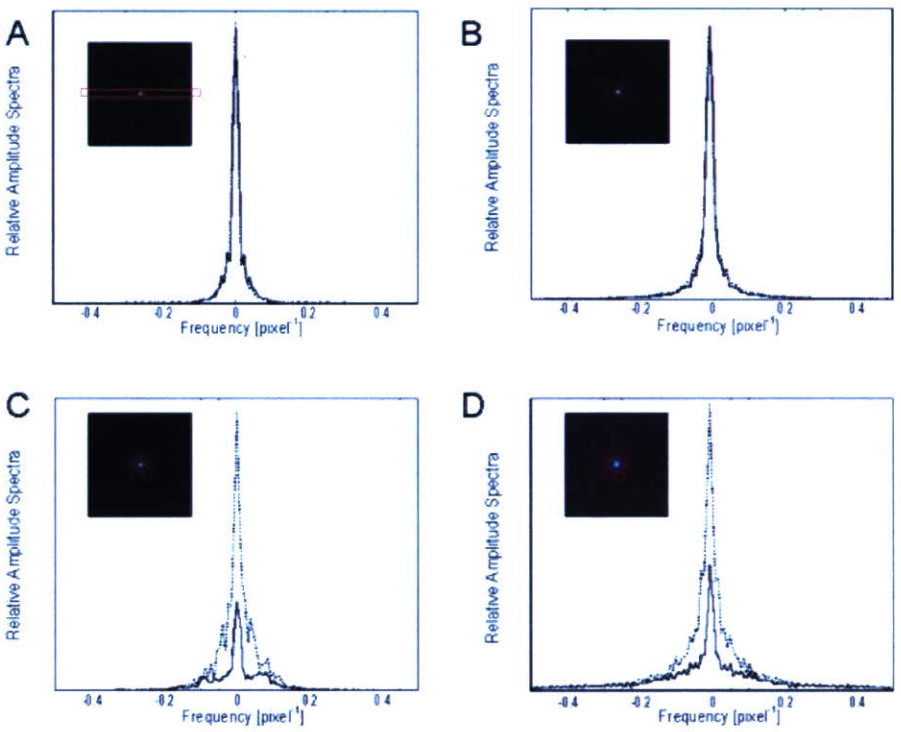

Fig. 3 Profiles of Fourier amplitude spectra from normal control (*solid line*) and Alzheimer's dementia patient (*dotted line*) calculated from SPECT image (A), 3DSSP image (B), Z-score of SPECT image (C) and Z-score of 3DSSP image (D). Individual profiles for the four types of image were obtained from the following images: images in (A) and (C) are transverse views at central slices of 3D Fourier amplitude spectra. Images in (B) and (D) are summed 2D Fourier amplitude spectra along eight individual slices of 3DSSP images.

Aging and Cancer, Tohoku University and there were no abnormalities on their MR images.[24] In this study, we randomly selected 10 controls (mean age, 64.8 ± 5.65 years) as the normal database for the calculation of Z-score, and the other 21 controls were used as test subjects for ROC analysis. We obtained informed consent from all AD patients or their next of kin. Written informed consent was obtained from all controls after a proper explanation of the study, in accordance with the Code of Ethics of the World Medical Association (Declaration of Helsinki).

SPECT study

SPECT study of cerebral perfusion was performed using *N*-isopropyl-[^{123}I]*p*-iodoamphetamine (IMP). All subjects received 111 MBq of the compound intravenously under standard resting conditions while lying supine on a scanning couch. The main projection data (158 keV ± 15%, 4 degree sampling) were acquired continuously for 30 min using a triple-head SPECT camera (Multispect3, Siemens, Malvern, PA, USA) with fan-beam collimators. The projection data were smoothed using a Butterworth filter (order 8 and a cutoff of 0.3 cycles/pixel) and reconstructed by FBP with a Ramp filter (10.6 mm FWHM of image resolution). Attenuation correction by Chang's method was applied assuming an attenuation coefficient of 0.08 cm^{-1}. Scatter correction was not performed.

Channelized Hotelling observer

A schematic diagram of CH observer is shown in Figure 1. CH observer accepts as an input an image f belonging to either a class of normal images, f_B, or a class of abnormal images (in this study, "abnormal" refers to AD), f_L, and provides the test statistic λ, which indicates the statistical index that determines whether the input image f falls in one group or the other.[13,14]

Initially, image f is converted by Fourier transformation. In frequency domain, filtering is applied for Fourier transformed image F (ρ) using radially symmetric channels $u_c(\rho)$ defined by the formula [21]

$$u_c(\rho) = \begin{cases} 1 \parallel \rho \parallel \in [\rho_0 2^{c-1}, \rho_0 2^c) \\ 0 \ \text{Otherwise} \end{cases},$$

$$r_c = \frac{\sum_\rho u_c(\rho) \cdot F(\rho)}{\sum_\rho u_c(\rho)} \qquad (1)$$

for c ∈{1,2,3,4,5}. By this filtering process, the channel matrix **r** (= [r_1, . . . , r_c]) is obtained. In this study, sets with the frequency cutoff ρ_0 (0.015, 0.02313, and 0.03125 pixel^{-1}) were tested. These were designated as the low-, mid-, and high-ρ_0 channel models, respectively. The cutoff ρ_0 values of 0.015 and 0.03125 were obtained from Gifford et al.[21] and Wollenweber et al.,[19] respectively, and 0.02313 is the mean of these two values. The test statistic λ of a CH observer for the task of detecting AD is as follows:

$$\lambda(\mathbf{f}) = \left[\overline{\mathbf{r}_L} - \overline{\mathbf{r}_B}\right]^T \mathbf{K}_U^{-1} \mathbf{r}, \qquad (2)$$

where r_L and r_B are the means of the two classes of channel matrices for the AD and control groups, respectively. The script "T" denotes a matrix transposition, and K_U is the c × c matrix averaged from the two-covariance matrices derived from channel matrices for the AD and control groups.

Image processing

As shown in Figure 2, we generated four types of images. A) SPECT images: After anatomical standardization by SPM 99, the normalization of global counts for each subject was set to 500 with proportional scaling. The matrix size of a SPECT image was 79 × 95 × 68 (2 × 2 × 2 mm^3). B) 3DSSP images: 3DSSP images (128 × 128; pixel size, 2.25 × 2.25 mm^2; and eight (projection) images) were processed according to a previous report,[12] where the maximum cortical activity was extracted adjacent to predefined surface pixels on a pixel-by-pixel basis, and the normalization of global counts for each subject was set to 500 with proportional scaling. C) Z-score images: The Z-value of SPECT images was calculated on a pixel-by-pixel basis with the following equation using SPECT images: Z = (mean of normalized pixel of normal database – normalized pixel of a patient)/SD of database. The normal database consisted of 10 controls as described in the previous section. D) Z-score of 3DSSP images: Z-score of 3DSSP images was calculated on a pixel-by-pixel basis using the equation described in C).

Image interpretation

We performed image interpretation using the four types of image for the differential diagnosis of AD patients from controls by human and CH observers.

Five experienced nuclear medicine physicians (4, 6, 8, 9, and 18 years of experience in brain nuclear medicine) were involved in the following four interpretation sessions: A) SPECT images: SPECT images in transverse (48 slices), sagittal (42 slices), and coronal planes (42 slices) were printed on two separate sheets. B) 3DSSP images: 3DSSP images were interpreted together with SPECT images. A 3DSSP image comprised eight projection images of the brain's surface and was printed on a sheet (Fig. 2B). C) Z-score images: Z-score images were interpreted together with SPECT images. A Z-score image (z ≥ 1) superimposed upon template MR images (Fig. 2C) was printed on two sheets in transverse, sagittal, and coronal planes. D) Z-score of 3DSSP images: Z-scores of 3DSSP images were interpreted together with SPECT and 3DSSP images. A Z-score of 3DSSP image (z ≥ 1) superimposed on a template MR image (Fig. 2D) was printed on a sheet. The nuclear medicine physicians were unaware of subject information or of predicted results, except for the information that the subjects comprised aged normal and AD patients. At the beginning of the

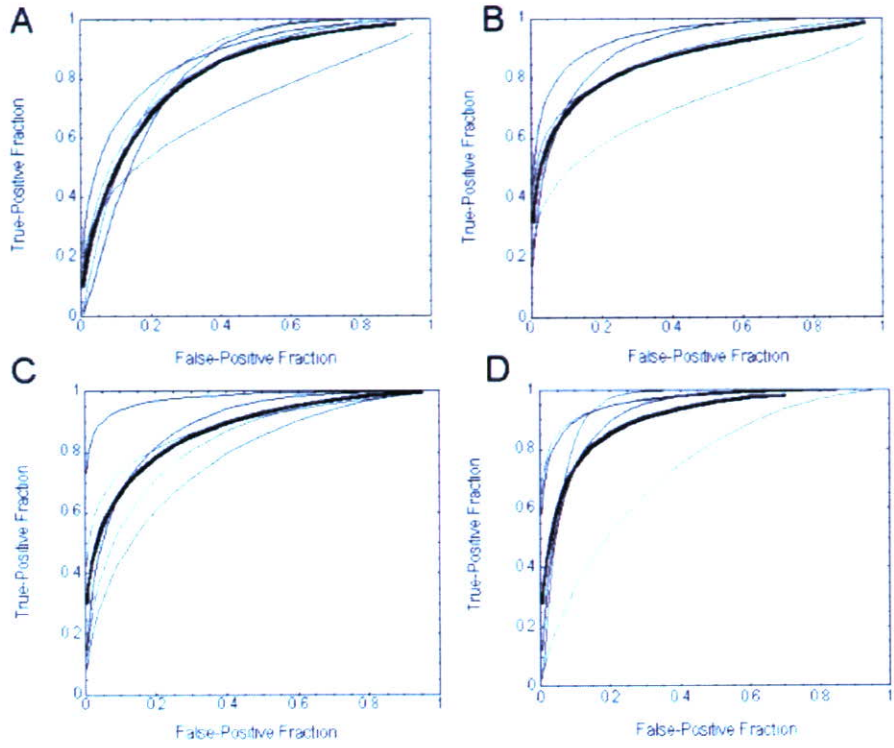

Fig. 4 Averaged (*bold solid lines*) and individual physician's (*thin solid lines*) ROC curves obtained from SPECT images (A), 3DSSP images (B), Z-scores of SPECT images (C) and Z-scores of 3DSSP images (D).

interpretation study, the nuclear medicine physicians received lectures, and practiced on one normal SPECT study and one study of a patient. The studies were not included in the study materials. Allotted time for the lecture and practice was 30 minutes in total. The lecture explained the typical SPECT findings in AD. The criteria were hypoperfusion of bilateral posterior cingulate gyri and precunei and/or hypoperfusion of bilateral medial-temporal and temporo-parietal lobes. Images were evaluated on a five-point scale of certainty: definitely, possibly, equivocally, possibly not, and definitely not. To avoid crossover interpretation artifacts, only one set of images was interpreted per session.

For the CH observer, the test statistics λ for all test images—A) SPECT images, B) 3DSSP images, C) Z-score images, and D) Z-score of 3DSSP images—were calculated and then a diagnosis was made after applying a fixed threshold value. First, all test images were converted into Fourier amplitude spectra and then channelized with a radial symmetric channeling filter using Eq. 1. The SPECT and Z-score images were performed using a 3D Fourier transform.[25] Because of slice independency, each slice of the 3DSSP and Z-score of 3DSSP images was processed using a 2D Fourier transform, and then Fourier amplitude spectra were summed along axial slices. The continuously distributed λ values of these test statistics for 42 test data (SPECT, Z-score, 3DSSP and Z-score of 3DSSP images) were used for the ROC analysis.

Data analysis

The human observer ratings data and continuously distributed CH observer data were analyzed using the ROCKIT 0.9.1 β program developed by Metz and coworkers (http://xray.bsd.uchicago.edu/krl).[26,27] This program fitted a binormal ROC curve to the given data using a maximum-likelihood technique, and then Az was estimated. Az was used as the measure of comparison between the human and CH observers for the four image types. Especially, correlations between averaged Az of human observer and Az of CH observer for four image types were statistically evaluated using the t-distribution of standardized r (Pearson's correlation coefficient).

RESULTS

Figure 3 shows the profiles of Fourier amplitude spectra for a control and an AD patient for the four types of image. Differences in spectra between AD and controls were quite small for SPECT and 3DSSP images. However, the profiles for controls and AD were quite separable for the Z-scores of the SPECT and 3DSSP images.

Figure 4 shows the ROC curves for SPECT, 3DSSP,

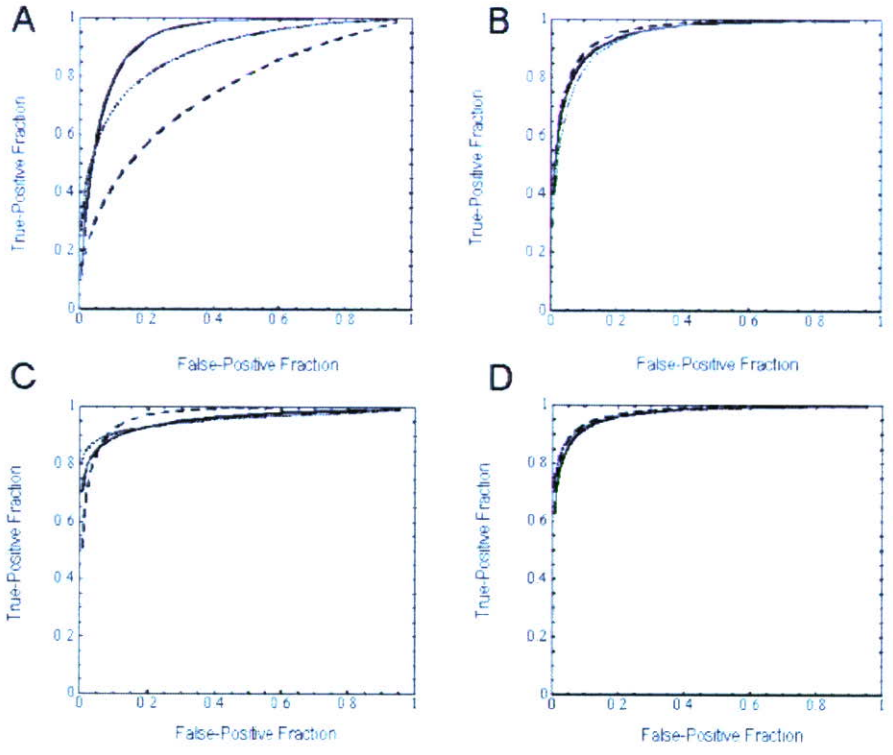

Fig. 5 ROC curves generated by CH observers with low- (*bold solid line*), mid- (*dotted line*), and high- (*dashed line*) channel models, and by averaged physicians (*thin solid lines*) from SPECT images (A), 3DSSP images (B), Z-scores of SPECT images (C) and Z-scores of 3DSSP images.

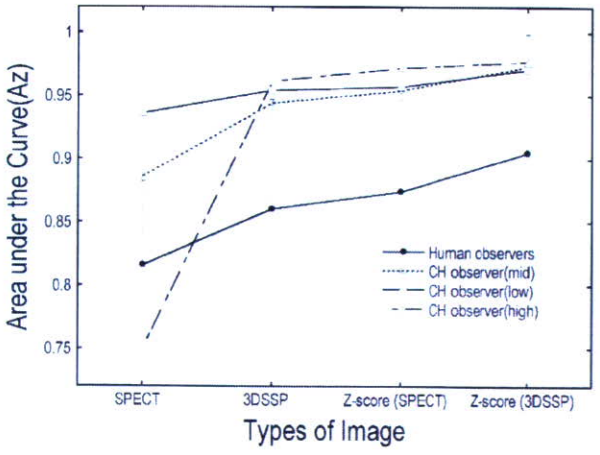

Fig. 6 Comparison of Az obtained by human and CH observers for four types of image. Error bars represent 1 SD for the results from the human observers (n = 5).

Z-score of SPECT, and Z-score of 3DSSP images as interpreted by the five physicians. The average performance of these human observers, as indicated by the average ROC curves, varied with the image type, and was generally better for Z-score images than for SPECT images, and was best for Z-score of 3DSSP images.

Figure 5 shows the ROC curves for SPECT, 3DSSP, Z-score of SPECT, and Z-score of 3DSSP images analyzed by the CH observers using the low-, mid-, and high-ρ_0 channel models in Eq. 1, compared with the averaged curve for the images analyzed by the five physicians. The performance of the CH observer in analyzing the SPECT images (Fig. 5A) was highly dependent on the definition of frequency cutoff values. This dependency was not observed in Figure 5B, C and D for the other image types.

Table 1 and Figure 6 show, respectively, a summary and a comparison of the averaged Az for the four image types as interpreted by the human and CH observers. Significant differences in Az obtained by human observers were observed between SPECT and Z-score of 3DSSP images ($p < 0.05$; paired t-test). CH observers on average performed better than the average human observer, as indicated by the Az values, with the exception of the CH observer that used a high-ρ_0 channel model for the SPECT images. In both groups, similar image-dependent trends were observed; that is, performance generally improved from the original SPECT images to the Z-score images of each respective data set. Pearson's correlation coefficient (r: index of linearity between two variables) for Az for the four image types between the average human and the CH observer using a mid-ρ_0, low-ρ_0 and high-ρ_0, channel model was 0.979, 0.997 and 0.887, respectively. There

Table 1 Summary of diagnostic performance of human observers with ROC analysis and CH observers with three frequency cutoff channel models. For human observers, mean ± 1 SD were calculated among individual Az values of 5 physicians

	SPECT	3DSSP	Z-score	Z-score of 3DSSP
Human observer	0.816 ± 0.066	0.860 ± 0.087	0.874 ± 0.073	0.905 ± 0.094
CHO-Low	0.936	0.954	0.957	0.971
CHO-Mid	0.886	0.944	0.957	0.973
CHO-High	0.750	0.961	0.972	0.977

were significant correlations between CH observer using a mid- and low-ρ_0 and human observers ($p < 0.05$).

DISCUSSION

In this study, we used a CH observer to segregate SPECT perfusion brain images of AD patients from those of controls. The performance of the CH observer was similar to that of the human observers.

The averaged ROC curve obtained by human observers was different among the four types of images shown in Figure 4. Az is 0.816 or 0.905 when either a SPECT image or the Z-score of a 3DSSP image is analyzed. This finding is consistent with that of Honda et al.,[11] who reported that the combined interpretation of the Z-score of a 3DSSP image and the SPECT image elicited an improved Az (0.778) compared with the interpretation of a SPECT image alone (0.679). The absolute values and magnitudes of changes in our study are different from those of Honda et al., perhaps due to differences in patient population (averaged MMSE score: 24 in Honda et al. and 21.6 in our study) and in the experience level of the nuclear medicine physicians.

Figure 5 and 6 show that the rank order of the four types of image processing by the CH observer was similar to that by the human observer. Significant correlations between human and CH observer were observed in condition with mid- and low-ρ_0 channel model. In particular, the performance of the CH observer with the mid-ρ_0 channel model was either close to or within 1 S.D. of human Az. Furthermore, the performance of the CH observer for the SPECT image (Fig. 5A) was heavily dependent on the frequency cutoff; this may be due to the characteristics of the frequency spectra of the SPECT images, which were distributed at the center as shown in Figure 3A.

Physicians focus on test images according to anatomical information and comparison with normal perfusion patterns experienced during previous diagnostic procedures. In contrast, the CH observer identifies frequency patterns on which it bases its inferences. Taking into account this mechanistic difference in image interpretation, the input images for human and CH observers were different in this study. Because statistically processed Z-score images lack anatomical information for the physician's interpretation, the Z-score images were thresholded and superimposed on template MR images (Fig. 2C and D). Additionally, the human observers always read the unprocessed SPECT images together with each processed image in three sessions. On the other hand, the CH observer identifies frequency characteristics and does not require any anatomical information. Therefore, the CH observer was able to work on a test target image alone without any additional information such as the MR template image and the setting of a threshold. The difference in input image for both human and CH observers makes this study unique from previous CH observer studies. Preliminary data suggest that the effects of the superimposed MR image and threshold value were negligible for the performance in the CH observer's analysis of Z-score images (data not shown).

In this study, the CH observer was implemented with 3D or 2D Fourier transformation for volumetric or surface-projection images, respectively. The CH observer with 2D Fourier transformation was originally developed in association with the human visual system on single-slice images.[13] 3D or 2D Fourier transformation with axial summation is used for multislice images[21,25]; however, there is no clear evidence showing any pertinent or obvious benefit of any technique. We assumed that when physicians interpret multislice brain perfusion SPECT images, they generate a mental image of three-dimensional images, and that this human interpretation is associated with 3D data handling. For this reason, we preferred to use 3D Fourier transformation for the multislice CH observer. However, whether 2D or 3D Fourier transformation generates a more accurate representation requires further investigation.[25]

Even though a significant correlation between the human and CH observers was observed, the CH observer with mid-ρ_0 and channel number 5 tends to overestimate the performance compared with the human observer. Another channel number for the CH observer or other numerical observer models, such as channelized non-pre-whitening (CNPW) and non-pre-whitening (NPW) observers,[19] may provide a more accurate prediction of the human observer.

The present approach may be useful for evaluating the effectiveness of a certain image processing technique. The current results suggest that although the SPECT images exhibited such dependence, yielding optimal results for the mid-ρ_0 channel model, statistically processed images may be relatively independent of such models.

However, it is unknown whether the independency of the frequency cutoff channels is observed for other conditions such that the optimization of frequency cutoff channels may be required.

This CH observer model with a frequency cutoff channel can be used to evaluate the effects of partial volume correction on statistically processed or unprocessed SPECT images.[28] Similarly, the effect of scatter correction for relative studies, such as is used in statistical analyses, has not yet been evaluated and may prove to be a useful substrate for further CH observer research.

CONCLUSION

The performance of the CH observer was similar to that of the human observers across all image types. This indicates that CH observer may be useful for evaluating image-processing methods in brain-perfusion SPECT.

ACKNOWLEDGMENTS

This work was supported in part by a Grant-in-Aid for Science Research from the Ministry of Education, Culture, Sports, Science and Technology, research grant 1420061 and a Grant-in-Aid for young researchers from the Association for Nuclear Technology in Medicine.

The authors are grateful to Hayato Odagiri of Tohoku University Hospital and Tachio Sato of IDAC, Tohoku University for data acquisition. The authors are also grateful to Babar Imran of IDAC, Tohoku University for helpful comments about the manuscript and discussion about data processing.

REFERENCES

1. Emilien G, Beyreuther K, Masters CL, Maloteaux JM. Prospects for pharmacological intervention in Alzheimer disease. *Arch Neurol* 2000; 57: 454–459.
2. Donnemiller E, Heilmann J, Wenning GK, Berger W, Decristoforo C, Moncayo R, et al. Brain perfusion scintigraphy with ^{99m}Tc-HMPAO or ^{99m}Tc-ECD and ^{123}I-beta-CIT single photon emission tomography in dementia of the Alzheimer-type and diffuse Lewy body disease. *Eur J Nucl Med* 1997; 24: 320–325.
3. Bonte FJ, Weiner MF, Bigio EH, White CL. Brain blood flow in the dementias: SPECT with histopathologic correlation in 54 patients. *Radiology* 1997; 202: 793–797.
4. Matsuda H. Cerebral blood flow and metabolic abnormalities in Alzheimer's disease. *Ann Nucl Med* 2001; 15: 85–92.
5. Imran MB, Awata S, Kawashima R, Sato K, Ito H, Ono S, et al. Follow-up of improvement in regional cerebral blood flow and mental status in Alzheimer's disease: A case report. *Clinic Nucl Med* 1998; 23: 601–603.
6. Imran MB, Kawashima R, Awata S, Sato K, Kinomura S, Ono S, et al. Parametric Mapping of Cerebral Blood Flow Deficits in Alzheimer's Disease: A SPECT Study Using HMPAO and Image Standardization Technique. *J Nucl Med* 1999; 40: 244–249.
7. Imran MB, Kawashima R, Sato K, Kinomura S, Ono S, Qureshy A, et al. Detection of CBF deficits in neuropsychiatric disorders by an expert system: A ^{99m}Tc-HMPAO brain SPET study using automated image registration. *Nucl Med Comm* 1999; 20: 25–32.
8. El Fakhri G, Kijewski MF, Albert MS, Johnson KA, Moore SC. Quantitative SPECT leads to improved performance in discrimination tasks related to prodromal Alzheimer's disease. *J Nucl Med* 2004; 45: 2026–2031.
9. Ishii K, Sasaki M, Matsui M, Sakamoto S, Yamaji S, Hayashi N, et al. A diagnostic method for suspected Alzheimer's disease using $H_2{}^{15}O$ positron emission tomography perfusion Z score. *Neuroradiology* 2000; 42: 787–794.
10. Imabayashi E, Matsuda H, Asada T, Ohnishi T, Sakamoto S, Nakano S, et al. Superiority of 3-dimensional stereotactic surface projection analysis over visual inspection in discrimination of patients with very early Alzheimer's disease from controls using brain perfusion SPECT. *J Nucl Med* 2004; 45: 1450–1457.
11. Honda N, Machida K, Matsumoto T, Matsuda H, Imabayashi E, Hashimoto J, et al. Three-dimensional stereotactic surface projection of brain perfusion SPECT improves diagnosis of Alzheimer's disease. *Ann Nucl Med* 2003; 17: 641–648.
12. Minoshima S, Frey KA, Koeppe RA, Foster NL, Kuhl DE. A diagnostic approach in Alzheimer's disease using three-dimensional stereotactic surface projection of fluorine-18-FDG PET. *J Nucl Med* 1995; 36: 1238–1248.
13. Myers KJ, Barrett HH. Addition of a channel mechanism to the ideal-observer model. *J Opt Soc Am A* 1987; 4: 2447–2457.
14. Yao J, Barrett HH. Predicting Human Performance by a Channelized Hotelling Observer Model. *Proc SPIE, Mathematical Methods in Medical Imaging* 1992; 1768: 161–168.
15. Barrett HH, Yao J, Rolland JP, Myers KJ. Model observers for assessment of image quality. *Proc Natl Acad Sci USA* 1993; 90: 9758–9765.
16. Qi Y, Tsui BM, Gilland KL, Frey EC, Gullberg GT. Evaluation of Parallel and Fan-Beam Data Acquisition Geometries and Strategies for Myocardial SPECT Imaging. *IEEE Trans Nucl Sci* 2004; 51: 667–672.
17. Farncombe TH, Gifford HC, Narayanan MV, Pretorius PH, Frey EC, King MA. Assessment of Scatter Compensation Strategies for ^{67}Ga SPECT Using Numerical Observers and Human LROC Studies. *J Nucl Med* 2004; 45: 802–812.
18. Sankaran S, Frey EC, Gilland KL, Tsui BM. Optimum Compensation Method and Filter Cutoff Frequency in Myocardial SPECT: A Human Observer Study. *J Nucl Med* 2002; 43: 432–438.
19. Wollenweber SD, Tsui BM, Lalush DS, Frey EC, LaCroix KJ, Gullberg GT. Comparison of Hotelling Observer Models and Human Observers in Defect Detection from Myocardial SPECT Imaging. *IEEE Trans Nucl Sci* 1999; 46: 2098–2103.
20. Gifford HC, King MA, de Vries DJ, Soares EJ. Channelized Hotelling and Human Observer Correlation for Lesion Detection in Hepatic SPECT Imaging. *J Nucl Med* 2000; 41: 514–521.
21. Gifford HC, King MA, Pretorius PH, Wells RG. A Comparison of Human and Model Observers in Multislice LROC Studies. *IEEE Trans Med Img* 2005; 24: 160–169.

22. McKhann C, Drachman D, Folstein M, Katzman R, Price D, Stadlan EM. Clinical diagnosis of Alzheimer's Disease: Report of the NINCDS-ADRDA work group under auspices of Department of Health and Human Services task force on Alzheimer's Disease. *Neurology* 1984; 34: 939–944.
23. Folstein MF, Folstein DE, McHugh PR. "Mini-mental state". A practical method for grading the cognitive state of patients for the clinician. *J Psychiatr Res* 1975; 12: 189–198.
24. Inoue K, Ito H, Shidahara M, Goto R, Kinomura S, Sato K, et al. Database of normal human cerebral blood flow measured by SPECT: II. Quantification of I-123-IMP studies with ARG method and effects of partial volume correction. *Ann Nucl Med* 2006; 20: 139–146.
25. Kim JS, Kinahan PE, Lartizien C, Comtat C, Lewellen TK. A comparison of Planar Versus Volumetric Numerical Observers for Detection Task Performance in Whole-Body PET Imaging. *IEEE Trans Nucl Sci* 2004; 51: 34–40.
26. Metz CE, Herman BA, Shen JH. Maximum-likelihood estimation of ROC curve from continuously-distributed data. *Stat Med* 1998; 17: 1033–1053.
27. Metz CE, Herman BA, Roe CA. Statistical comparison of two ROC curve estimates obtained from partially-paired datasets. *Med Decis Making* 1998; 18: 110–121.
28. Kanetaka H, Matsuda H, Asada T, Ohnishi T, Yamashita F, Imabayashi E, et al. Effects of partial volume correction on discrimination between very early Alzheimer's dementia and controls using brain perfusion SPECT. *Eur J Nucl Med* 2004; 31: 975–980.